Rock and Soil Mechanics

Volume 44 | Issue 6 Article 8

10-3-2023

Mechanism of liquefaction-induced lateral spreading in liquefiable inclined sites

Ke-min JIA
Key Laboratory of Urban Security and Disaster Engineering of the Ministry of Education, Beijing University of Technology, Beijing 100124, China, jiakemin6@163.com

Cheng-shun XU
Key Laboratory of Urban Security and Disaster Engineering of the Ministry of Education, Beijing University of Technology, Beijing 100124, China

Xiu-li DU
Key Laboratory of Urban Security and Disaster Engineering of the Ministry of Education, Beijing University of Technology, Beijing 100124, China

Xiao-ling ZHANG
Key Laboratory of Urban Security and Disaster Engineering of the Ministry of Education, Beijing University of Technology, Beijing 100124, China

See next page for additional authors

Follow this and additional works at: https://rocksoilmech.researchcommons.org/journal

 Part of the Geotechnical Engineering Commons

Recommended Citation

JIA, Ke-min; XU, Cheng-shun; DU, Xiu-li; ZHANG, Xiao-ling; SONG, Jia; and SU, Zhuo-lin (2023) "Mechanism of liquefaction-induced lateral spreading in liquefiable inclined sites," *Rock and Soil Mechanics*: Vol. 44: Iss. 6, Article 8.
DOI: 10.16285/j.rsm.2022.6053
Available at: https://rocksoilmech.researchcommons.org/journal/vol44/iss6/8

This Article is brought to you for free and open access by Rock and Soil Mechanics. It has been accepted for inclusion in Rock and Soil Mechanics by an authorized editor of Rock and Soil Mechanics.

Mechanism of liquefaction-induced lateral spreading in liquefiable inclined sites

Authors

Ke-min JIA, Cheng-shun XU, Xiu-li DU, Xiao-ling ZHANG, Jia SONG, and Zhuo-lin SU

This article is available in Rock and Soil Mechanics: https://rocksoilmech.researchcommons.org/journal/vol44/iss6/8

Rock and Soil Mechanics 2023 44(6): 1837−1848 ISSN 1000−7598
https: //doi.org/10.16285/j.rsm.2022.6053 http://rocksoilmech.researchcommons.org/journal

Mechanism of liquefaction-induced lateral spreading in liquefiable inclined sites

JIA Ke-min[1], XU Cheng-shun[1], DU Xiu-li[1], ZHANG Xiao-ling[1], SONG Jia[1, 2], SU Zhuo-lin[1]
1. Key Laboratory of Urban Security and Disaster Engineering of the Ministry of Education, Beijing University of Technology, Beijing 100124, China
2. School of Civil Engineering, North China University of Technology, Beijing 100144, China

Abstract: A numerical model of the liquefaction horizontal free-field shaking table test was developed based on the completed large-scale shaking table test of liquefaction horizontal free field using the OpenSees finite element platform, and the numerical model was verified. Based on this, a free-field numerical model of the overall inclined foundation was established, and the non-cyclic dynamic response of the liquefaction lateral spreading site and the mechanism of liquefaction-induced lateral spreading were discussed. The results show that the established numerical model can effectively simulate the seismic response in liquefiable sites. There was significant relative displacement at the interface between liquefiable loose sand and overlying non-liquefiable layer. In the inclined site, the strain accumulation of saturated sand soil starts from the upper part of the loose sand layer and gradually develops downward. The increase of excess pore water pressure was not completely coupled with the accumulation of non-cyclic strain of the soil. The non-cyclic lateral displacement was controlled by the middle parts of the site. In the process of soil liquefaction, when the shear stress along the sliding surface is less than the initial static shear stress, lateral spreading starts, and the shear stress ratio of the saturated loose sand layer is in the range of 0.04−0.06, which is slightly smaller than the initial static shear stress ratio. In addition, it is found that liquefaction-induced lateral spreading requires a certain site inclination (greater than 0.5º). The lateral displacement of soil conforms to the cosine distribution pattern. With the increase of site inclination, the contribution of liquefiable deep soil to the overall lateral displacement is more significant.
Keywords: liquefaction; lateral spreading; free filed; numerical simulation; seismic response; mechanism; shaking table test

1 Introduction

Seismic damage investigation results show that ground lateral spreading caused by vibration liquefaction of saturated sandy soil is one of the main causes of structural damage in the liquefaction zone[1−3]. A typical example is the liquefaction and cracking on both sides of the Shinano River in the 1964 Niigata earthquake in Japan. The maximum ground displacement at the Yachiyo bridge and Showa bridge reached 12.71 m, and a large number of buildings, bridges and lifeline projects were severely damaged[4]. Sandy soil liquefaction and lateral spreading were found in the 1999 Kocaeli earthquake in Turkey, the 1999 Chi-chi earthquake in Taiwan, China, the 2010 Chile earthquake, the 2011 Christchurch earthquake in New Zealand, the 2014 Greece earthquake, and the 2021 Mado earthquake in Qinghai in China[5−10]. The massive liquefaction slip in the 7.5 magnitude earthquake in Sulawesi Province, Indonesia in 2018 caused great damage to people's lives and properties[11]. Therefore, the liquefaction-induced lateral spreading under earthquake has become an important research hotspot in the field of earthquake engineering. The earthquake damage investigation results show that the liquefaction-induced lateral spreading mainly occurs in near-shore horizontal sites and slightly inclined sites, so the investigation of the seismic response of liquefaction and lateral spreading mechanism of the slightly inclined free-field site is the basis for the study of the seismic damage mechanism of liquefaction-induced lateral spreading site structures.

Aiming at the above earthquake damages, many scholars have studied the lateral deformation of liquefiable soils using experiments and numerical simulations. Xu et al.[12] revealed the law of the influence of skeleton density and fine grain content on the shear modulus and damping ratio in the large deformation stage of liquefaction flow through laboratory cyclic torsional shear tests. Wei et al.[13] used particle flow software to model the cyclic shear test of saturated sand, and discussed the mesoscopic mechanism of large deformation of saturated sand after liquefaction from the perspective of soil pore distribution. However, due to the inherent limitations of the unit test, it is limited in studying the mechanism of lateral deformation of liquefaction. Sasaki et al.[14] studied the effects of surface slope, the inclination angle of the bottom of the liquefaction layer, the thickness of the liquefaction layer, and sand

Received: 6 July 2022 Accepted: 26 October 2022
This work was supported by the General Program of National Natural Science Foundation of China (52078016), the National Natural Science Foundation for Outstanding Young Scholars of China (51722801) and the General Program of Beijing Natural Science Foundation (8192012).
First author: JIA Ke-min, male, born in 1993, PhD, majoring in liquefaction of saturated sandy soil and seismic resistance of pile foundation.
E-mail: jiakemin6@163.com
Corresponding author: XU Cheng-shun, female, born in 1977, PhD, Professor, PhD supervisor, research interests: soil dynamics and geotechnical earthquake engineering. E-mail: xuchengshun@bjut.edu.cn

density on the lateral displacement of the liquefaction site through a series of shaking table tests, and believed that the lateral deformation only occurred in the liquefaction layer. Wang et al.[15] combined seismic investigations, in-situ tests, laboratory tests, and numerical simulations to explore the mechanism of large-scale seismic liquefaction slips in loess strata. Chen et al.[16] realized the static simulation of lateral spreading of sand under zero effective stress, focusing on the influence of sandy foundation inclination angle and relative compactness on lateral spreading, and found that the inclination angle had a significant effect on lateral spreading. However, it has little effect on the slope degree of the final deformation surface of the soil. To provide more accurate control data for numerical models, based on the liquefaction experiments and analysis projects, Zhou et al.[17] and Kokkali et al.[18] conducted centrifuge shaker tests on inclined liquefiable sites and explored the dynamic response of the inclined sites. In addition, Xu et al.[19−20] carried out large shaking table tests of a liquefiable horizontal free field and its pile-structure system to explore the seismic response law of the soil-structure system. Further, Jia et al.[21] designed and carried out a series of large shaking table tests on inclined liquefiable site-group pile-bridge systems to provide necessary data support to reveal the liquefied lateral large deformation and its seismic failure mechanism of the pile-bridge system. However, shaking table model tests are characterized by long duration, high cost, and large discreteness, and it is impractical to conduct a large number of experimental studies. With the development of computer technology, the use of numerical simulation methods that can reflect the liquefaction process and soil failure mechanism is increasingly favored by scholars.

Through the numerical simulation, Elgamal et al.[22] constructed a multi-yield surface plastic constitutive model capable of describing the properties of liquefiable soils and also used a solid-liquid coupled finite element program to analyze the effects of soil pore pressure, shear dilatation, and other factors on the lateral spreading of liquefiable soils. On the basis of above investigations, Elgamal et al.[23] established a 3D finite element model based on the open-source finite element software OpenSees to analyze the lateral deformation of the inclined liquefiable site and evaluated the effect of pile driving in the soil layer to slow down the lateral deformation of the soil. Cai et al.[24] used a modified softening modulus method to simulate the liquefaction-induced lateral large deformation of nearshore caisson shore walls and soils in the 1995 Kobe earthquake and explored the mechanism of liquefaction-induced lateral large deformation in nearshore horizontal sites. Wang et al.[25] simplified the three-dimensional free field into a one-dimensional shear beam calculation model and analyzed the effects of ground inclination, relative compactness of sand soil, different seismic wave characteristics, and peak acceleration on the lateral deformation of the ground surface, and obtained some useful conclusions. Dong et al.[26] proposed a liquefaction-induced large deformation constitutive model for the dynamic response analysis of liquefiable sites. In addition, Zhao et al.[27] analyzed the liquefaction characteristics of offshore horizontal sites. Zhuang et al.[28] established a finite element model of the liquefiable inclined sites to reveal the characteristics of soil liquefaction distribution, lateral deformation, and ground settlement.

The results of the above model tests and numerical simulations show that factors such as soil compactness, permeability coefficient, surface slope, liquefiable layer thickness, vibration intensity, and holding time have a great influence on the lateral spreading of liquefiable inclined sites. However, there is a lack of systematic analysis of the mechanism of liquefiable lateral spreading. On the other hand, compared with the *Japanese Specification of Seismic Design for Highway Engineering*(2002)[29], the *Chinese Specification of Seismic Design for Highway Engineering* (JTG B 02—2013)[30] does not have clear provisions on the calculation method of liquefiable lateral spreading displacement and measures to resist liquefied lateral spreading displacement. Therefore, it is necessary to conduct further research on issues such as the mechanism of liquefiable lateral spreading in saturated sand sites.

In this study, we establish a two-dimensional finite element model of liquefiable horizontal free-field for the liquefiable free-field large shaking table test completed by the author's team in the early stage and verify the validity of the numerical model based on the shaking table test results. Based on this, a model of a liquefiable inclined site is established to discuss the dynamic response and liquefaction-induced lateral spreading mechanism of a liquefiable inclined site.

2 Numerical model verification

Based on the results of the large shaking table test of liquefiable horizontal free field carried out by the author's team, the saturated soil is simulated as a two-phase medium with complete solid-liquid coupling based on Boit porous media theory. A two-dimensional liquefiable site numerical analysis model is established, and the reliability of the numerical model is verified by comparing the calculated results with the experimental results.

2.1 Shaking table test

The liquefaction horizontal free-field shaking table test was completed at the Institute of Earthquake Engineering

of China Academy of Building Research. A rectangular laminated shear model soil box was used for the test, and the overall dimensions of the model foundation were 3.2 m× 2.4 m×2 m(length×width×height), and the corresponding foundation soil layers and sensors were laid out as shown in Fig. 1. The foundation soil layers were composed of 0.5 m dense sand layer, 1.2 m liquefiable saturated loose sand layer, and 0.3 m clay overburden layer from bottom to top, and the soil layers were prepared by a modified water-sinking method[31]. The site soil was prepared and left to consolidate naturally for 24 h, and the water level was kept flush with the upper surface of the clay layer. The details of the shaking table test and the physical parameters of the site soil are described in literature[19, 32]. The Wolong earthquake records of the Wenchuan earthquake were selected as the input ground motion for the test, and the PGA was adjusted to 0.3*g*. The acceleration time−history records are shown in Fig. 2. The test mainly measures the acceleration and pore pressure of the soil.

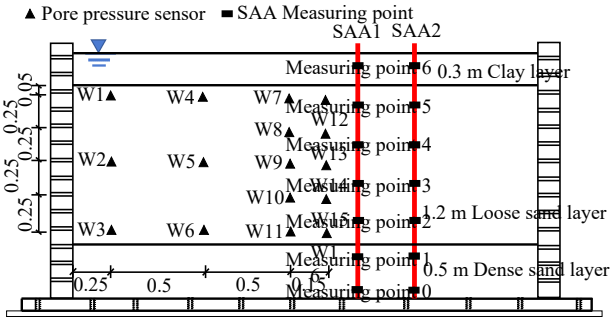

Fig. 1 Sensor layout of shaking table test(unit: m)

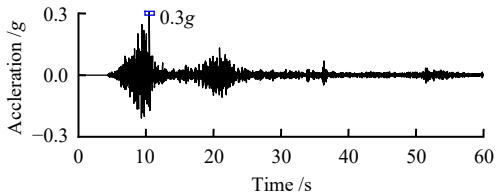

Fig. 2 Acceleration time history recorded at Wolong station of Wenchuan earthquake

2.2 Model establishment

Based on the open-source finite element calculation platform OpenSees, a two-dimensional finite element calculation model of the shaking table test was established, and the pre- and post-processing processes were carried out in GID software. The finite element discrete model is shown in Fig. 3.

The saturated soil was simulated using quadrilateral plane strain element quapUP. Based on Biot's porous media theory, this type of element simulated saturated sand as a two-phase medium. The Biot formula was discretized into *u*−*p* form[33], where *u* is the displacement

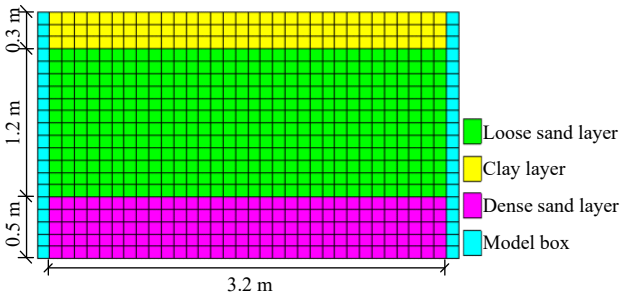

Fig. 3 Finite element discrete model of shaking table test

of soil particles, *p* is the pore water pressure, and the *u*−*p* form could consider the interaction between pore water pressure and soil skeleton. A multi-yield surface plastic constitutive model[34], which is more sensitive to pore water pressure changes, was used for saturated sandy soils, and it corresponds to the PDMY02 model in the OpenSees materials database, which can better simulate the dilation and flow of sandy soils under cyclic loading and can reproduce the shear deformation accumulation and liquefaction characteristics during the dynamic process. A multi-yield surface plastic constitutive model[35] that was insensitive to pore water pressure changes, is adopted for clay, and the model corresponds to the PIMY model in the OpenSees materials database. The relative density D_r and void ratio *e* of saturated sand were the parameters given in the shaking table test[32, 36]. According to the method recommended by Kramer et al.[37] for taking model parameters, the other parameters in the model were obtained from the calibration values and the suggested values of the model developer using linear interpolation of the relative densities[38−39]. The site soil parameters are listed in Table 1. The shear model box in the 1*g* shaking test had a certain weight, and the model box was inclined to produce a certain lateral force on the soil body along the slope direction. To consider the influence of the model box, the quadrilateral solid element quad was used to simulate each layer of the model box frame and assign its mass stiffness and other information, while interlayer element of each layer of the model box was constructed to realize the free sliding of laminar shear type box in the horizontal direction. The established laminar shear box model schematic is shown in Fig. 4.

In addition, the numerical model considers the shear localization that occurs near the interface between the saturated sand and the overlying clay under strong earthquakes. This phenomenon has been observed several times in past experiments and it was noted that this problem deserves focused attention[40−42]. In the numerical model, a zero-length element ZeroLength was set along the interface direction to link the relative motion conditions at the

interface of different materials, and the strength of the interface element was coupled with the effective stress of the underlying loose sand. The initial shear strength of the interface element was equal to the drainage shear strength of the underlying loose sand element, and after the sand was liquefied, the shear strength of the interface element was approximately equal to the strength of the underlying sand. In the direction perpendicular to the interface, a rigid spring element was selected to transfer the gravity of the upper clay layer to the lower sand layer.

Table 1 Parameters of soil model

Name of soil layer	ρ/(kg • m^{-3})	G_r/kPa	B_r/kPa	c/kPa	φ/(°)	γ_{max}	p_{res}/kPa	d	Number of yield surfaces	ϕ_{PT}/(°)	c_1
Clay layer	1 500	18 000	70 000	30	0	0.1	100	0.0	20	—	—
Dense sand layer	1 900	75 700	220 000	—	37	0.1	101	0.5	—	28.5	0.045
Loose sand layer	1 700	45 900	150 000	—	31	0.1	101	0.5	—	24.0	0.087

Notes: ρ is the density; G_r is the reference shear modulus; B_r is the reference bulk modulus; c is the cohesion; φ is the internal friction angle; γ_{max} is the peak strain; p_{res} is the reference confining pressure; d is pressure coefficient; ϕ_{PT} is the phase transition angle; c_1 is the contraction parameter.

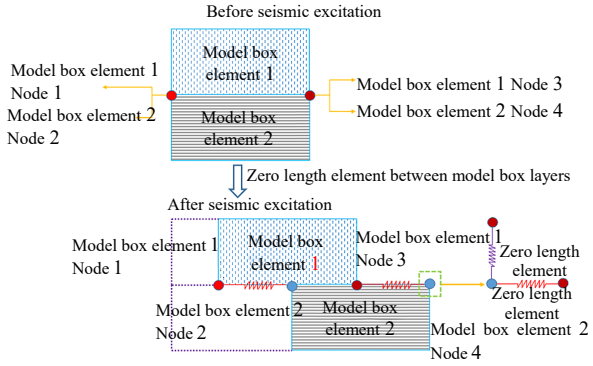

Fig. 4 Schematic diagram of laminar shear box model

The surface of the model was set as a free permeable boundary condition, and the bottom and both sides were set as impermeable boundary conditions. The corresponding nodes on both sides of the surface boundary in the vibration direction were set up with bundling constraints by the EqualDOF command to keep the displacement of the corresponding boundary nodes in each layer consistent. The finite element analysis process consists of the following two steps:

(1) In the gravity loading stage, a shaking table free-field saturated soil model is established, and a quadrilateral plane strain cell was used for finite element meshing of the saturated soil. The displacement and freedom degrees of pore pressure of the nodes at the interface between the loose sand layer and the clay layer were bound and the boundary conditions were imposed. The permeability coefficient of the saturated soil layer was set to 1 for rapid consolidation of the soil. The elastic and plastic gravity analyses were performed to generate the initial stress fields.

(2) The soil deformation in the gravity analysis stage was set to be 0, while the permeability coefficient of the saturated soil was updated to a set value, ground vibrations were applied, and the solution was integrated into the time domain using the Newmark integration method. A set of 3% Rayleigh damping was used at the low strain level to ensure the computational stability of the dynamic analysis.

2.3 Model reliability verification

The validity of the numerical model was verified by comparing the shaking table test results of the horizontal liquefiable site with the calculated results. The acceleration time history curves of the numerical results of SAA2-0, SAA2-2, and SAA2-5 at different depths of the site soil and the experimental results are given in Fig. 5, and it can be observed that the experimental and calculated results show basically the same variation pattern. From the acceleration peaks of SAA2-0 and SAA2-2 measured in the test, it can be seen that the acceleration peaks of the loose sand layer show an obvious attenuation compared with those of the underlying dense sand layer, and the numerical calculation can also simulate the attenuation of the acceleration peaks of the loose sand layer.

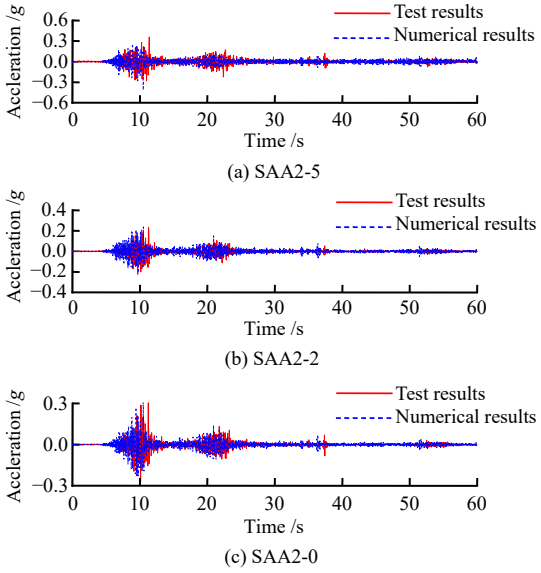

Fig. 5 Acceleration time histories at SAA2 measuring point

Figure 6 compares the experimental and the numerical results of the excess pore pressure in the loose sand layer.

It shows the numerical results reproduce the phenomenon of pore pressure growth during the vibration process. During the seismic excitation process, the time-history response trends of the excess pore water pressure in the test results and the numerical results are basically the same, and the time of peak occurrence also basically coincides.

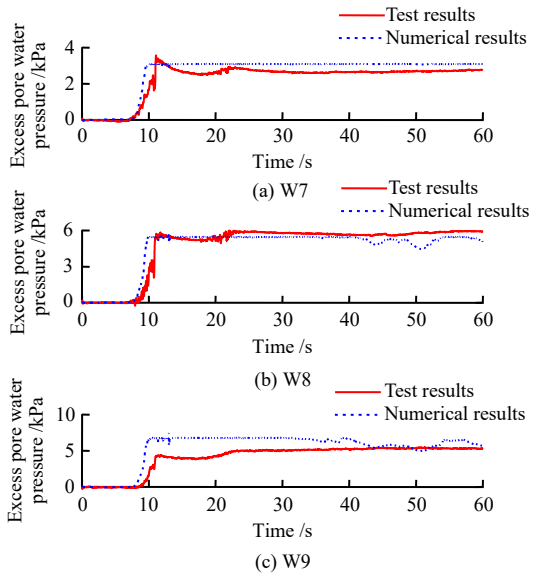

Fig. 6 Time history of excess pore pressure at measuring points in loose sand layer

3 Dynamic response analysis

In this section, a numerical model of a lateral spreading shaking table test on a liquefiable site with inclination of 2° was established based on the aforementioned numerical modelling method, and the dynamic analysis steps were the same as those for a horizontal site. In general, the thickness from the surface of the soil layer to the bedrock reaches tens of meters, and the distribution characteristics of the liquefiable layer are also complicated. To realize the lateral spreading of earthquake-induced liquefaction and ensure the reliability of the numerical model as much as possible, this study has not considered the influence of soil thickness, but only changed the inclination angle of the site, focusing on the analysis of the overlying clay layer with initial static shear stress, the middle saturated loose liquefiable lateral spreading mechanism of a typical site profile of the sand layer and the lower dense sand layer. On the whole, the lateral spreading begins within 5−10 s of the seismic excitation input, and the following analysis focuses on the dynamic response during this time period.

3.1 Excess pore water pressure response

Figure 7 shows the time history curves of excess pore water pressure ratio of saturated sand within the period of 5−10 s. Figure 8 shows the distribution of the excess pore pressure of the soil along the depth at different times. It can be seen from Figs. 7 and 8 that the pore pressure of the soil at the positions of 0.4, 0.7, and 1.0 m from the surface increases to the maximum value at t = 7.5 s, and still keeps build-up at the positions of 1.3, 1.6 and 1.9 m from the surface, indicating that the liquefiable shallow layer is liquefied first under the earthquake, and the liquefaction speed of the deep layer is slower than that of the shallow layer. With the increase of burial depth, the amplitude of the pore pressure ratio of saturated sand decreases gradually, which shows a typical liquefaction pattern: the liquefaction first starts in the shallow layer of saturated sandy soil and then develops downward. On the other hand, the pore pressure ratio amplitudes of the loose sand layer (0.4, 0.7, 1.0, 1.3 m from the surface) are all greater than 0.8, while the pore pressure ratio amplitudes of the dense sand layer (1.6, 1.9 m from the surface) do not exceed 0.8.

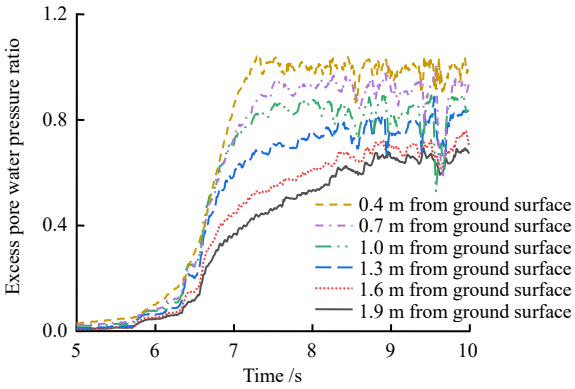

Fig. 7 Time histories of excess pore pressure ratio in saturated sand layer

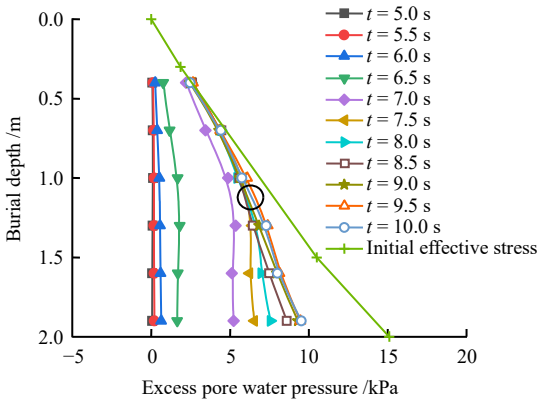

Fig. 8 Distribution of excess pore water pressure along buried depth at different times

3.2 Lateral spreading displacement

Figure 9 shows the time histories of lateral displacement of soil at different buried depths. It can be obviously found that the amplitude of lateral displacement decreases with the increase of buried depth. Figures 10 and 11 show the

lateral displacement time history curves and the enlarged displacement time history curves of the soil within the time period of 5−10 s. It is observed that there is almost no lateral displacement of the soil in the period of 5−7 s; the lateral displacement begins to accumulate slowly at t = 7 s; after t = 7.5 s, the lateral displacement of the loose sand shallow layer and the middle soil increase rapidly; after t = 8 s, the lateral displacement of the soil near the bottom of loose sand increases significantly.

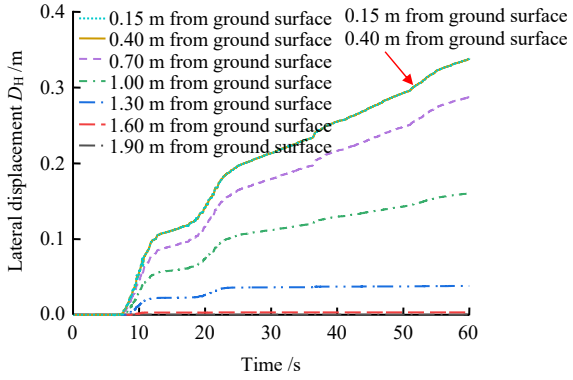

Fig. 9 Lateral displacement time histories of soil with different buried depth

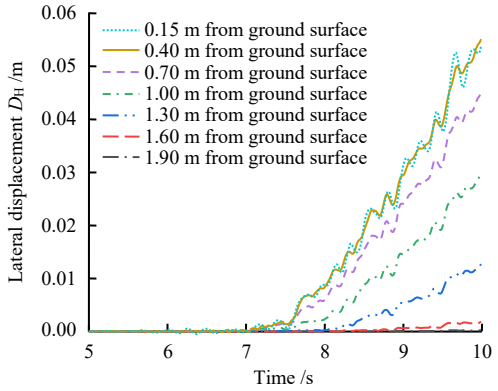

Fig. 10 Lateral displacement time histories of soil in 5−10 s

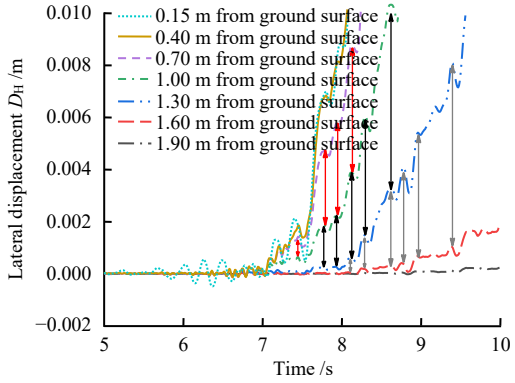

Fig. 11 Enlarged lateral displacement time histories of soil in 5−10 s

The calculated lateral displacement of the site is decomposed into two parts, the cyclic component generated by vibration and the non-cyclic component closely related to the liquefaction-induced lateral spreading. Figure 12 is the time history curves of soil non-cyclic lateral displacement. From Figs. 9 to 11, it can be seen that before t = 7 s, the displacement response of the soil is mainly a cyclic component, and the non-cyclic displacement rapidly accumulates after t = 7 s, and when t = 10 s, the non-cyclic displacement of the foundation surface accumulates to 5.5 cm.

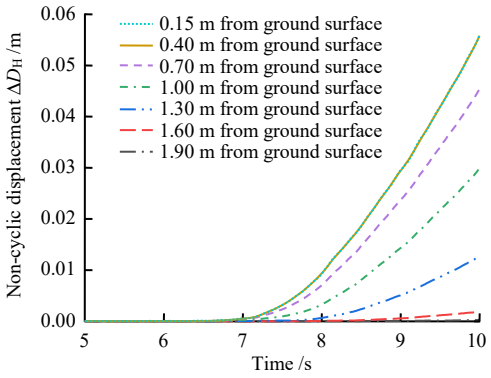

Fig. 12 Non-cyclic displacement time histories of soil with different depths

The lateral displacement clouds of the site soil at different moments are given in Fig. 13, where the effect of displacement deformation is magnified by a factor of 5. As seen in Fig.13, the lateral deformation initiates from the shallow layer of loose sand (t = 8 s). After the significant occurrence of lateral deformation, a more obvious relative displacement is observed near the clay−loose sand interface. The reason may be that the excess pore water accumulated in saturated loose sand under strong seismic forces seeps upwards and is obstructed by the low permeability overlying the clay layer at the soil interface, as a result, the pore water accumulates at the soil interface, causing a relative displacement between the overlying clay layer and the saturated sand layer at their interface. It should be noted that the lateral displacement of the overlying clay layer at the soil−loose sand interface is smaller compared with that of the saturated sand layer at t = 9.56 s, while it is larger than that of the saturated sand layer at t = 9.65 s. This may be attributed to the reduced friction between the saturated loose sand layer and the overlying clay layer interface after liquefaction. In this case, the inertia of the overlying clay layer causes an oscillatory, which leads to a change in the direction of the lateral relative displacement.

3.3 Soil strain

Figure 14 depicts the total shear strain response time curves of the soil. It can be seen from the figure that the total shear strain of the soil at burial depths of 0.4, 0.7, and 1.0 m starts to accumulate at the time of t = 7 s, while

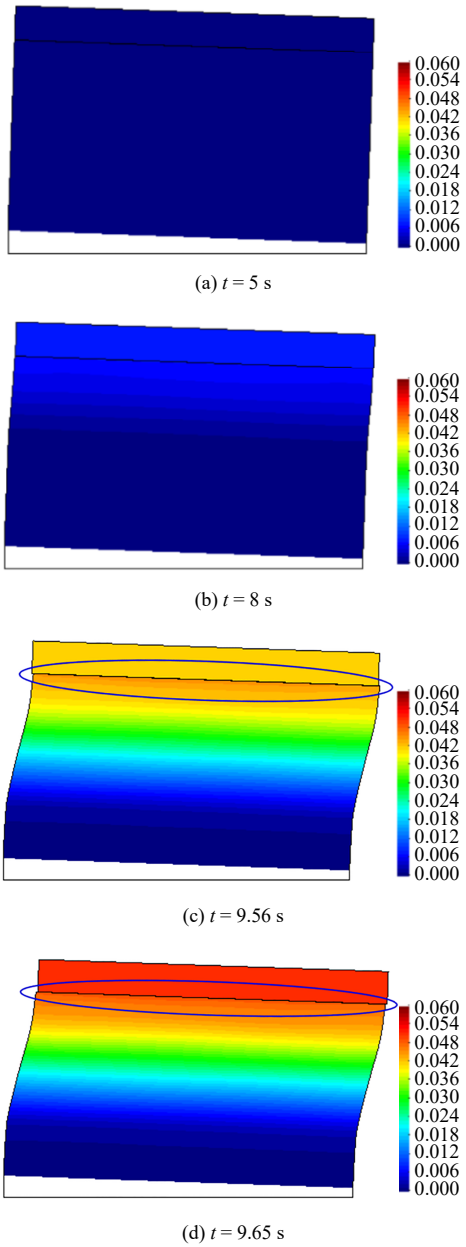

Fig. 13 Contour plot of lateral displacement of soil at different moments (unit: m)

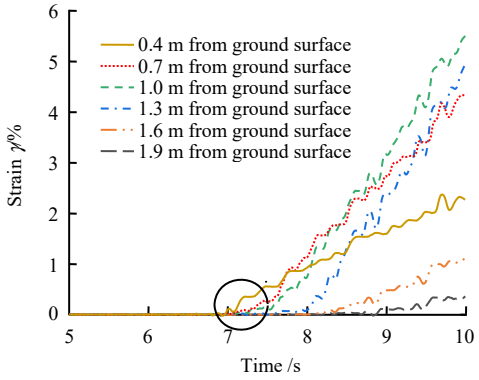

Fig. 14 Soil strain time history within 5−10 s

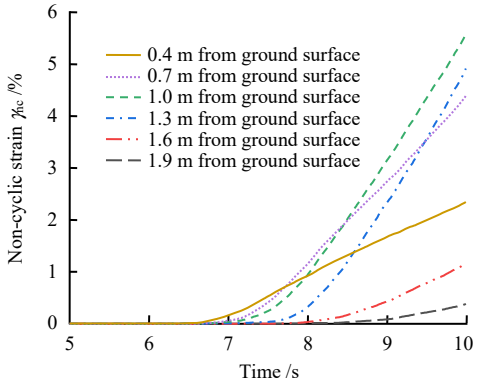

Fig. 15 Non-cyclic strain time history of soil within 5−10 s

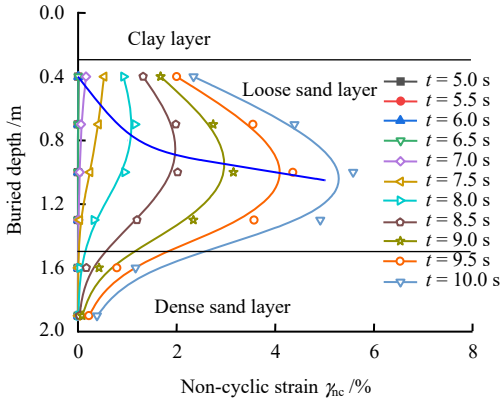

Fig. 16 Relationship between soil non-cyclic strain and buried depth at different moments

the strain of the soil at burial depth of 1.3 m gradually accumulates at t = 8 s. Moreover, the accumulation rates of strains in different soil layers are not consistent. The acyclic strain time history curves of the soil is given in Fig. 15. It demonstrates that the accumulation of non-cyclic strain in the soil starts from the shallow layer of saturated loose sand and gradually progresses to the deep layer until the bottom of the foundation. It is noteworthy that the accumulation rates of acyclic strain in soils with different burial depths are, in descending order, 1.3, 1.0, 0.7, 0.4, 1.6, and 1.9 m. The relationship between the acyclic strain in soils and the burial depth at different moments is given in Fig. 16. Obviously, the non-circulatory strain of the soil at the burial depth of 0.4 m is the largest at t = 7 s and gradually develops to the deeper layers with time.

4 Lateral spreading mechanism

The saturated sandy soil of the inclined liquefiable site is divided into five layers, and the percentage of each layer to the overall non-cyclic lateral displacement is given in Table 2. As can be seen from the table, the percentages of soil layers 1 to 5 to the overall non-cyclic displacement are 19%, 28%, 31%, 19%, and 3%. It indicates that the middle of the loose sand layer controls the development of lateral spreading displacement, and the shallow layer of the loose sand and clay layer are more passive in the process of liquefaction-induced lateral spreading. The bottom dense sand layer is not liquefied, and its contribution

to the lateral spreading process is limited.

Table 2 Contribution of layered sand soil to overall lateral displacement

Soil layer number	Burial depth /m	Layer thickness ΔH /m	Non-cyclic lateral spreading displacement response (5−10 s)		
			Non-cyclic displacement ΔD_H /m	Accumulated non-cyclic displacement D_H /m	Percentage $\beta = \Delta D_H / D_H$ /%
1	0.4−0.7	0.3	0.010 38	0.055 60	19
2	0.7−1.0	0.3	0.015 53	0.045 22	28
3	1.0−1.3	0.3	0.017 13	0.029 69	31
4	1.3−1.6	0.3	0.010 89	0.012 56	19
5	1.6−1.9	0.3	0.001 67	0.001 67	3

As can be seen from Fig. 14, the strains in soil layers 2 and 3 are smaller before t = 7 s. At t = 7.5 s, the strains in the soils at burial depths of 0.4, 0.7, and 1.0 m accumulate to 0.53%, 0.41%, and 0.24%, and the pore pressure ratios of the corresponding soils exceed 0.8. In contrast, the strains in the soils at burial depths of 1.3 and 1.6 m are 0.03% and 0.003%, and the pore pressure ratios of the corresponding saturated sandy soils are 0.7 and 0.6. It is worth noting that the strain accumulation rates of the soil at the burial depths of 1.0 and 1.3 m are faster.

As seen in Figs. 15 and 16, the strain in the soil at the burial depth of 0.4 m accumulates from 0.53% at 7.5 s to 0.92% at t = 8 s, and the strain rate is 0.78%/s; the strain rates in the soil at the burial depths of 0.7, 1.0, and 1.3 m are 1.48%/s, 2.2%/s, and 2.3%/s, and the strain rates are basically constant from 8 to 10 s. The strains of the soil at the burial depths of 1.6 and 1.9 m still keeps smaller. It should be noted that the non-cyclic lateral strains of the soil at burial depths of 1.6 and 1.9 m start to accumulate after 8.5 s and 9 s, and the accumulated strain rates are 0.76%/s and 0.33%/s, and this is because the dense sand has not liquefied.

The above analysis shows that liquefiable inclined sites accumulate high pore water pressure in the saturated loose sand layer under seismic loading, which leads to the liquefaction-induced lateral spreading and large displacement of the soil. This mechanism occurs simultaneously with the generation of high strains in liquefiable soils, and as liquefaction progresses from the upper part to the lower part, the high-strain region subsequently develops towards the lower part of the soil but pore pressure ratio and strain are not fully coupled. It is shown that the non-cyclic lateral strain in the deep saturated loose sand is higher than that in the shallow layer, but the pore pressure ratio in the deep sand is smaller than that in the shallow sand.

4.1 Shear stress

Figure 17 gives a schematic diagram of the forces acting on the assumed sliding surface in the lateral spreading soil. As can be seen from the figure, the force along the sliding surface before input of ground motion consists of the component of the soil gravity above the sliding surface in the direction of the sliding surface and the soil interface shear force T. We define the driving static shear stress $\tau_{static} = T/A$, where A is the area of the sliding surface. In contrast to horizontal liquefiable sites, the driving static shear stress exists in inclined liquefiable sites to keep the liquefied lateral spreading site in equilibrium. The shear stress at the sliding surface is changed after the liquefaction of a saturated sand site, breaking the equilibrium state of the forces along the sliding surface.

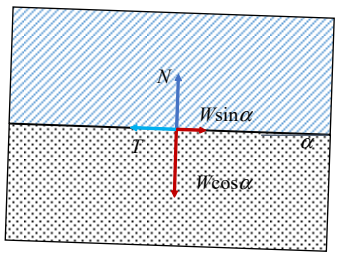

Fig. 17 Schematic diagram of force acting on sliding surface

Figure 18 shows the non-cyclic shear stress time histories in the soil at different depth ranges. The non-cyclic shear stresses of the soil remain slightly increases in the time period from 5 to 6 s. This may be due to the slight increase in the shear stress of the soil due to the small vibration effect. The shear stress of the soil in the range of burial depth 0.4 to 1.3 m gradually decreases, which is attributed to the difference in the pore pressure accumulation rate of the soil at different depths (see Fig. 7). The shear stress of the soil at burial depths of 1.6 and 1.9 m increases slightly and has no decreasing trend because the pore pressure ratio of the soil in the lower dense sand layer always remains less than 0.8 and no liquefaction occurs. It is worth noting that the sliding event occurs at t = 7 s, but the rapid accumulation time of displacement

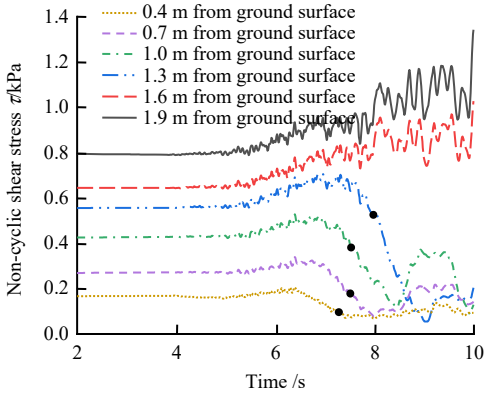

Fig. 18 Non-cyclic shear stress time histories

is observed at t = 7.5 s. It indicates that large soil displacements may be induced once the shear stress of the soil falls below the initial value of shear stress (t = 5 s).

As can be seen in Fig. 18, there exists a more obvious recovery of soil shear stress at burial depths of 0.7 and 1.0 m in the time period of 8.5 to 9 s, but it does not return to the initial value of shear stress, and after about 0.5 s, it decreases to a lower level again. This phenomenon is related to the shear dilation[43], which was also observed in a previous experimental studies[44]. The non-cyclic shear stress−strain relationships for soils with different burial depths are shown in Fig. 19, where the shear stress decreases significantly with increasing non-cyclic shear strain in soils at burial depths of 0.4 to 1.3 m. The difference is that the non-cyclic shear strains at the burial depths of 0.4, 0.7, 1.0, and 1.3 m are 0.5%, 1.0%, 2.0%, and 2.5%, when the soil shear stress decreases to the minimum value, after which the non-cyclic shear stresses recover with the increase of non-cyclic shear strains and the significant shear dilation can be observed in saturated sandy soil.

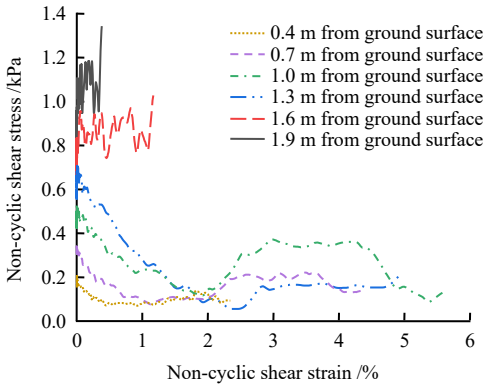

Fig. 19 Relationship between non-cyclic shear stress and strain

4.2 Shear strain ratio

The shear stress along the sliding surface of the soil before the input of ground motion is defined as the static shear stress τ_0, the ratio of the static shear stress to the initial effective stress is the static shear stress ratio, and the ratio of the shear stress to the initial effective stress after the input of ground motion is the shear stress ratio. Table 3 gives the shear stress ratio and static shear stress ratio for the accumulation of non-cyclic strain at each buried soil depth. As can be seen from the table, the range of shear stress ratio at non-cyclic strain accumulation is 0.04 to 0.06, which is smaller than the initial static shear stress ratio at the corresponding depth.

The above analysis shows that during the softening process of the soil, once the shear stress along the sliding surface drops to the initial static shear stress of the soil at the corresponding depth, the sliding may be triggered. It can be seen from Fig.7 that the necessary condition for the liquefaction-induced lateral spreading is that the pore pressure ratio reaches 0.8.

Table 3 Shear stress ratio of soils with different depths during non-cyclic strain accumulation

Start time of non-cyclic strain /s	Buried depth /m	Initial effective stress σ_{v0} /kPa	Static shear stress τ_0 /kPa	Shear stress τ/kPa	Static shear stress ratio τ_0/σ_{v0}	Shear stress ratio τ/σ_{v0}
7.1	0.4	2.28	0.166	0.115	0.073	0.044
7.5	0.7	4.44	0.274	0.194	0.062	0.041
7.6	1.0	6.60	0.425	0.380	0.064	0.055
8.0	1.3	8.76	0.556	0.532	0.064	0.058

5 Influence of inclination angle

Figure 20 presents the displacement time histories of the soil at the burial depth of 0.4 m for different site inclination angles. It can be observed from the figure that the lateral displacement of the soil has a tendency to increase gradually with the increase of the inclination angle of the site. It is noted that the lateral displacement of the soil is not significant when the site is horizontal or inclined at an angle of 0.5°. Significant lateral displacements are observed at site inclination angles ranging from 0.8° to 4°. It shows that under the earthquake, the liquefaction of the saturated sandy soil site and the induction of lateral spreading require the site to have a certain inclination angle. The driving static shear stress in the site soil with a small inclination angle is tiny. When the lateral spreading starts, the shear stress of the soil along the sliding surface is required to be less than the driving static shear stress, which requires that the shear strength of the soil in the liquefied state is sufficiently small. It can be seen from Fig. 18 that the soil shear stress significantly decreases under strong earthquake excitation, but it is not infinitely close to a sufficiently small value. Therefore, it is reasonable to speculate that when the inclination angle of the site is small (less than 0.5°), there is little possibility of significant lateral spreading under strong earthquakes.

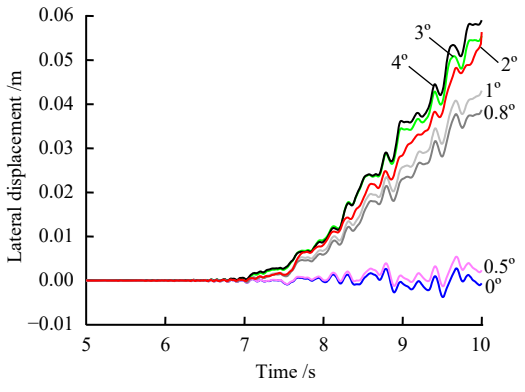

Fig. 20 Displacement time histories of 0.4 m deep soil at different inclination angles

Figure 21 illustrates the distribution of soil displacement amplitude along the buried depth when the site has different inclination angles. The figure shows that the dense sand layer does not show significant lateral displacement. With the increase of site inclination angle, the amplitude of lateral displacement of the loose sand layer at different depths increases gradually. When the site is horizontal and the inclination angle is 0.5°, the amplitude of the permanent lateral displacement of the soil is significantly smaller than that of sites with other inclination angles, indicating that the site with a sufficiently small inclination angle is less likely to experience significant lateral spreading when subjected to an earthquake. On the other hand, according to previous studies, there are two situations in the displacement distribution of soil: linear mode and cosine mode[45]. Figure 21 also shows the comparison between the soil displacement distribution and previous studies when the inclination angle of the site is 4°. It is observed that the lateral permanent displacement distribution matches the cosine mode, and is quite different from the linear mode. The lateral displacement distribution when the site is inclined from 0.8° to 3° is basically the same as that at 4°. It is speculated that the displacement distribution of the lateral spreading of soil induced by liquefaction conforms to the cosine mode.

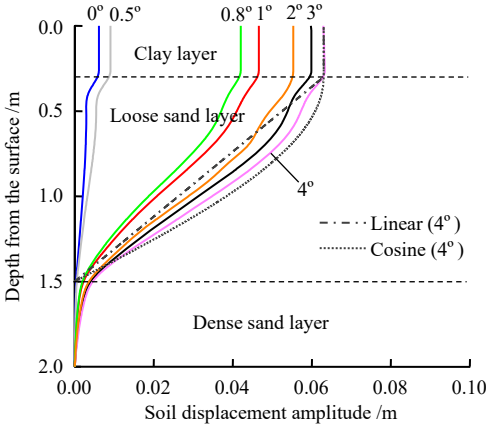

Fig. 21 Displacement profile of soil at different inclination angles

Figure 22 shows the distribution of the strain amplitude of the soil when the site is inclined at different angles. With the increase of inclination angle, the shear strain amplitude of the soil increases gradually. The soil exhibits limited shear strain amplitude when the site is horizontal or the inclination angle is 0.5°. As the inclination angle increases, significant shear strain amplitudes are observed, especially in the middle of the loose sand layer. It is worth noting that when the inclination angle increases, the position of the maximum shear strain amplitude of the soil moves from the middle of the loose sand layer to the deep layer.

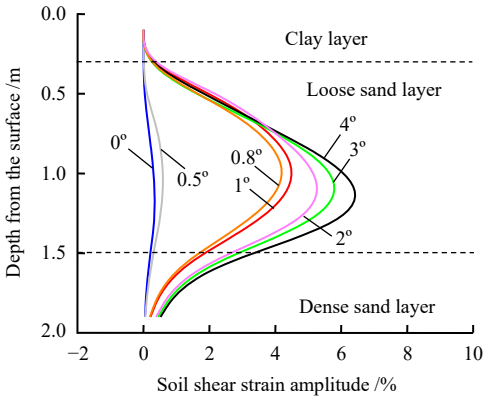

Fig. 22 Strain amplitude distribution of soil at different inclination angles

Figure 23 gives the contribution of layered soils to the overall lateral displacement at different inclination angles. Similar to the law when the inclination angle of the site is 2° in Table 2, the soil near the middle of the loose sand layer contributes most significantly to the overall lateral displacement. It is worth noting that as the inclination angle increases, the contribution of the deep layer of loose sand (0.7−1 m) to the overall displacement gradually increases, while the contribution of the shallow layer of loose sand gradually decreases, which is similar to the distribution of the strain amplitude of the soil (see Fig. 22). It shows that the contribution of the deep layer of liquefiable loose sand to the overall lateral displacement becomes more and more significant when the inclination angle of the site increases.

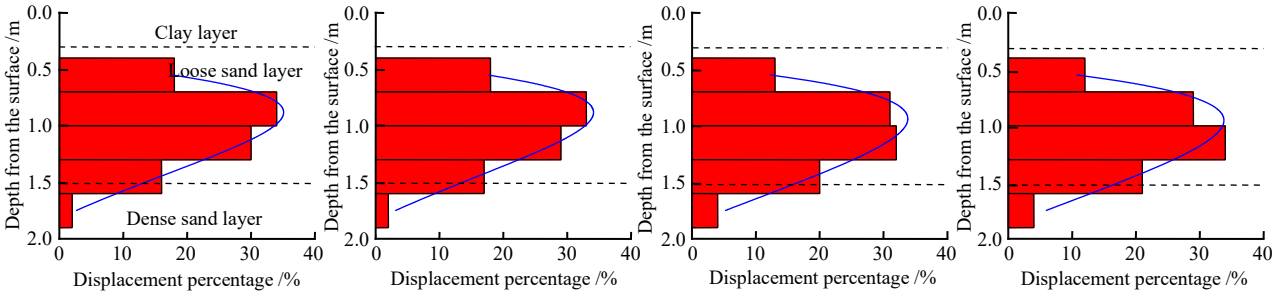

(a) Inclination angle of site is 0.8° (b) Inclination angle of site is 1° (c) Inclination angle of site is 3° (d) Inclination angle of site is 4°

Fig. 23 Proportion of soil displacement at different inclination angles

6 Conclusion

In this study, the reliability of the liquefiable free-field seismic response simulation method was verified by establishing a numerical model of the liquefiable horizontal free-field shaking table test. Based on this, a numerical model of the liquefaction-inclined free-field shaking table test was established. The dynamic response of the liquefiable site where lateral spreading occurs and the mechanism of lateral spreading initiation were analyzed, and the following conclusions were drawn:

(1) The non-cyclic strain accumulation of soil starts from the shallow layer and gradually develops to the deep layer. The accumulative rate of non-cyclic strain in the middle and lower layers of saturated loose sand is faster and controls the development of non-cyclic lateral displacement. The growth of excess pore water pressure and the accumulation of non-cyclic strain in soil do not show a coupling phenomenon. In addition, it is also found that there is an obvious relative displacement at the interface between the saturated loose sand and the overlying clay layer.

(2) During the liquefaction of saturated sandy soil, the shear stress along the sliding surface decreases, and sliding starts when the shear stress decreases below the initial static shear stress, and the liquefaction-induced lateral spreading phenomenon occurs. The shear stress ratio ranges from 0.04 to 0.06 for the accumulated non-cyclic shear strain in each layer of soil, which is slightly less than the initial static shear stress ratio at the corresponding depth.

(3) Saturated sand liquefying and inducing lateral spreading require the site to have a certain inclination angle (greater than 0.5^{o}). The liquefaction-induced lateral displacement distribution conforms the cosine pattern. The contribution of liquefiable deep soil to the overall lateral displacement becomes more and more significant as the inclination angle of site increases.

References

[1] LIAM F W D. A study of piles during earthquakes: issues of design and analysis[J]. Bulletin of Earthquake Engineering, 2005, 3(2): 141−234.

[2] LING Xian-chang, TANG Liang. Recent advance in seismic analysis for bridge foundations in liquefaction-induced lateral spreading soils[J]. Earthquake Engineering and Engineering Dynamics, 2015, 35(1): 1−10.

[3] XU Cheng-shun, JIA Ke-min, DU Xiu-li, et al. Review on seismic behavior of pile foundation subjected to liquefaction induced lateral spreading[J]. Journal of Disaster Prevention and Mitigation Engineering, 2021, 41(4): 768−791.

[4] HAMADA M, TOWHATA I, YASUDA S, et al. Study on permanent ground displacement induced by seismic liquefaction[J]. Computers and Geotechnics, 1987, 4(4): 197−220.

[5] SONMEZ B, ULUSAY R, SONMEZ H. A study on the identification of liquefaction-induced failures on ground surface based on the data from the 1999 Kocaeli and Chi-Chi earthquakes[J]. Engineering Geology, 2008, 97(3-4): 112−125.

[6] YENP W, CHEN G D, BUCKLE I, et al. Bridge performance during the 2010 M8. 8 Chile earthquake[C]//Structures Congress. Las Vegas, Nevada: ASCE, 2011: 1649−1659.

[7] HASKELL J J M, MADABHUSHI S P G, CUBRINOVSKI M, et al. Lateral spreading-induced abutment rotation in the 2011 Christchurch earthquake: observations and analysis[J]. Géotechnique, 2013, 63(15): 1310−1327.

[8] PALERMO A, WOTHERSPOO L, WOOD J, et al. Lessons learnt from 2011 Christchurch earthquakes[J]. Bulletin of the New Zealand Society for Earthquake Engineering, 2011, 44(4): 319−333.

[9] ATHANASOPOULOS G A, KECHAGIAS G C, ZEKKOS D, et al. Lateral spreading of ports in the 2014 Cephalonia, Greece, earthquakes[J]. Soil Dynamics and Earthquake Engineering, 2020, 128: 105874.

[10] YUAN J, WANG Y, ZHAN B, et al. Comprehensive investigation and analysis of liquefaction damage caused by the Ms7. 4 Maduo earthquake in 2021 on the Tibetan Plateau, China[J]. Soil Dynamics and Earthquake Engineering, 2022, 155: 107191.

[11] SASSA S, TAKAGAWA T. Liquefied gravity flow-induced tsunami: first evidence and comparison from the 2018 Indonesia Sulawesi earthquake and tsunami disasters[J]. Landslides, 2019, 16(1): 195−200.

[12] XU Cheng-shun, PAN Xia, FENG Chao-qun, et al. Experimental research on dynamic shear characteristics of liquefaction circulating flow soil[J]. China Civil Engineering Journal, 2020, 53(3): 95−102.

[13] WEI Xing, ZHANG Zhao, WANG Gang, et al. DEM study of mechanism of large post-liquefaction deformation of saturated sand[J]. Rock and Soil Mechanics, 2019, 40(4): 1596−1602, 1625.

[14] SASAKI Y, TOKIDA K, MATSUMOTO H, et al. Experimental study on lateral flow of ground due to soil liquefaction[C]// Proceedings of the 2nd International Conference on Recent Advances in Geotechnical Earthquake and Soil Dynamics. Missouri: [s. n.], 1991: 263−270.

[15] WANG Lan-min. Mechanism and risk evaluation of sliding flow triggered by liquefaction of loess deposit during earthquakes[J]. Chinese Journal of Geotechnical Engineering, 2020, 42(1): 1−19.

[16] CHEN Y, XU C, LIU H, et al. Physical modeling of lateral spreading induced by inclined sandy foundation in the state of zero effective stress[J]. Soil Dynamics and Earthquake Engineering, 2015, 76: 80−85.

[17] ZHOU Y, SUN Z, CHEN Y. Zhejiang University benchmark centrifuge test for LEAP-GWU-2015 and liquefaction responses of a sloping ground[J]. Soil Dynamics and Earthquake

Engineering, 2018, 113: 698−713.

[18] KOKKALI P, ABDOUN T, ZEGHAL M. Physical modeling of soil liquefaction: overview of LEAP production test 1 at Rensselaer Polytechnic Institute[J]. Soil Dynamics and Earthquake Engineering, 2018, 113: 629−649.

[19] XU Cheng-shun, DOU Peng-fei, DU Xiu-li, et al. Large-scale shaking table model test of liquefiable free field[J]. Rock and Soil Mechanics, 2019, 40(10): 3767−3777.

[20] XU Cheng-shun, DOU Peng-fei, DU Xiu-li, et al. Dynamic response analysis of liquefied site-pile group foundation-structure system-large-scale shaking table model test[J]. Chinese Journal of Geotechnical Engineering, 2019, 41(12): 2173−2181.

[21] JIA Ke-min, XU Cheng-shun, DU Xiu-li, et al. Experimental design of shaking table tests for seismic failure response of pile-group-superstructure subjected to liquefaction-induced lateral spreading[J]. Engineering Mechanics. DOI: 10.6052/j.issn.1000-4750.2021.11.0922.

[22] ELGAMAL A W, YANG Z. Numerical modeling of liquefaction-induced lateral spreading[C]//Proceedings of the Twelfth World Conference on Earthquake Engineering. Auckland: [s. n.], 2000.

[23] ELGAMAL A, LU J, FORCELLINI D. Mitigation of liquefaction-induced lateral deformation in a sloping stratum: three-dimensional numerical simulation[J]. Journal of Geotechnical and Geoenvironmental Engineering, 2009, 135(11): 1672−1682.

[24] CAI Xiao-guang, YUAN Xiao-ming, LIU Han-long. Mechanism and softening modulus approach for liquefaction induced lateral spreading of ground near river bank or seashore[J]. Earthquake Engineering and Engineering Dynamics, 2005, 25(3): 125−131.

[25] WANG Hao, GAO Guang-yun, WANG Yu. Study on lateraling spreading of liquefiable and inclined ground under earthquake[C]// Proceedings of 2016 National Engineering Geology Academic Annual Conference. Beijing: Science Press, 2016: 102−109.

[26] DONG Qing, ZHOU Zheng-hua, SU Jie, et al. A constitutive model considering post-liquefaction deformation based on the logarithmic skeleton curve[J]. Rock and Soil Mechanics, 2021, 42(7): 1903−1910.

[27] ZHAO Liu-yuan, SHAN Zhi-gang, WANG Ming-yuan. Analysis of liquefaction characteristics of horizontal site of offshore wind farm under earthquake in the South Yellow Sea[J]. Rock and Soil Mechanics, 2022, 43(1): 169−180, 194.

[28] ZHUANG Hai-yang, YANG Jing, CHEN Su, et al. Liquefaction performance and deformation of slightly sloping site in floodplains of the lower reaches of Yangtze River[J]. Ocean Engineering, 2020, 217: 107869.

[29] Japan Road Association(JRA). Specifications for high-way bridges, part V: seismic design[S]. Tokyo: Public Works Research Institute and Civil Engineering Research Laboratory, 2002.

[30] Ministry of Transport of the People's Republic of China. JTG B 02−2013 Code for seismic design of highway engineering[S]. Beijing: China Communications Press, 2014.

[31] ISHIHARA K. Liquefaction and flow failure during earthquakes[J]. Geotechnique, 1993, 43(3): 351−451.

[32] XU Cheng-shun, DOU Peng-fei, DU Xiu-li, et al. Experiment study on seismic response of superstructure-piles-soils system-design of test plan for large scale shaking table model experiments[J]. Journal of Disaster Prevention and Mitigation Engineering, 2019, 39(3): 365−374, 411.

[33] LI G, MOTAMED R. Finite element modeling of soil-pile response subjected to liquefaction-induced lateral spreading in a large-scale shake table experiment[J]. Soil Dynamics and Earthquake Engineering, 2017, 92: 573−584.

[34] YANG Z, ELGAMAL A, PARRA E. Computational model for cyclic mobility and associated shear deformation[J]. Journal of Geotechnical and Geoenvironmental Engineering, 2003, 129(12): 1119−1127.

[35] ELGAMAL A, YANG Z, PARRA E. Computational modeling of cyclic mobility and post-liquefaction site response[J]. Soil Dynamics and Earthquake Engineering, 2002, 22(4): 259−271.

[36] XU C S, DOU P F, DU X L, et al. Seismic performance of pile group-structure system in liquefiable and non-liquefiable soil from large-scale shake table tests[J]. Soil Dynamics and Earthquake Engineering, 2020, 138: 106299.

[37] KRAMER S L, ARDUINO P, SHIN H S. Using OpenSees for performance-based evaluation of bridges on liquefiable soils[R]. Berkeley: Pacific Earthquake Engineering Research Center, 2008.

[38] KHOSRAVIFAR A, BOULANGER R W, KUNNATH S K. Effects of liquefaction on inelastic demands on extended pile shafts[J]. Earthquake Spectra, 2014, 30(4): 1749−1773.

[39] YANG Z, LU J, ELGAMAL A. OpenSees soil models and solid-fluid fully coupled elements user's manual[R]. California: University of California, San Diego, 2008.

[40] MALVICK E J, KUTTER B L, BOULANGER R W. Postshaking shear strain localization in a centrifuge model of a saturated sand slope[J]. Journal of Geotechnical and Geoenvironmental Engineering, 2008, 134(2): 164−174.

[41] CHANG D, BOULANGER R, BRANDENBERG S, et al. FEM analysis of dynamic soil-pile-structure interaction in liquefied and laterally spreading ground[J]. Earthquake Spectra, 2013, 29(3): 733−755.

[42] WANG X, LUO F, SU Z, et al. Efficient finite-element model for seismic response estimation of piles and soils in liquefied and laterally spreading ground considering shear localization[J]. International Journal of Geomechanics, 2017, 17(6): 06016039.

[43] ZEGHAL M, ELGAMAL A W. Analysis of site liquefaction using earthquake records[J]. Journal of Geotechnical Engineering, 1994, 120(6): 996−1017.

[44] ZAYED M, EBEIDO A, PRABHAKARAN A, et al. Asymmetric input motion for accumulation of lateral ground deformation in laminar container shake table testing[J]. Canadian Geotechnical Journal, 2021, 58(2): 210−223.

[45] TOKIMATSU K, ASAKA Y. Effects of liquefaction-induced ground displacements on pile performance in the 1995 Hyogoken-Nambu earthquake[J]. Soils and Foundations, 1998, 38: 163−177.